The design and performance of an effusive gas source of conical geometry for photoionization studies

D. P. Seccombe,[a] S. A. Collins, and T. J. Reddish
Physics Department, Newcastle University, Newcastle-upon-Tyne, NE1 7RU, United Kingdom

(Received 29 January 2001; accepted for publication 28 March 2001)

The design, construction, and performance of an effusive gas source of conical geometry is reported. This gas jet enables experiments that require the gas and photon beams to be essentially collinear and has a focusing multicapillary array with the central portion left free for the photon beam. In total, the source comprises 90 ''tubes'' in three layers and has been designed by modeling free molecular gas flow and optimizing for highest gas density ~2–3 mm from the jet's exit plane. The nature of the gas flow through the source and its focusing properties are investigated theoretically and experimentally. © *2001 American Institute of Physics.* [DOI: 10.1063/1.1373667]

I. INTRODUCTION

Gas phase photoelectron spectroscopy experiments usually require a relatively small and well-defined interaction region of high gas density. This region needs to be located away from any sources of secondary emission (i.e., metal surfaces) to reduce low energy background counts. A conventional experiment employs a long, narrow tube that admits gas into the vacuum chamber perpendicularly to the direction of the photon beam [Fig. 1(a)]. This geometry allows the tip of the tube to be kept away from the photon beam without withdrawing it too far from the interaction region. There have been many attempts to improve upon the ''hypodermic needle'' as an effusive source, the most successful being variations on the multicapillary array design.[1–19] By employing many small tubes it is possible to improve the collimation of the gas flow and thereby have greater control on the density profile.

In recent years there has been a rapid increase in the size and complexity of electron and ion analyzers, and coincidence experiments utilizing two or more of these devices have become increasingly popular. Furthermore, the desire to perform angle- and energy-resolved experiments probing processes with low cross sections has led to the development of systems that facilitate multiplex data collection using sophisticated analyzers and position-sensitive detectors. These advances have often led to a decrease in the available space around the interaction region. The perpendicular arrangement of the gas and photon beams, despite its advantages, prevents the entire 360° being used for detection purposes [see Fig. 1(a)]. A coaxial geometry [Fig. 1(b)], where the photon beam and gas molecules enter the system along the same path, would overcome this difficulty. This is not straightforward, however, since it results in a long interaction region with the highest gas density close to the metal surfaces of the gas inlet. This work describes the design, construction, and initial performance of a coaxial gas injection system that takes all these considerations into account. The principles of the design have general applicability to other kinds of gas-phase experiments.

The details of the original apparatus have been reported elsewhere.[20] Briefly, a dual toroidal electron spectrometer was designed to study electron–electron coincidences arising from photodouble ionization (PDI). The angular acceptances of the two toroidal analyzers are 180° and 100°, respectively, and the electron detection plane is perpendicular to the direction of the photon beam [Fig. 2(a)]. The omitted 70° sector enabled gas to be admitted into the chamber via a hypodermic needle located within the detection plane. Due to the recent desire to detect one of the fragment ions produced as a result of molecular PDI (e.g., $h\nu + D_2 \rightarrow 2D^+ + 2e^-$) *in addition* to the two electrons, a conventional cylindrical electrostatic ion analyzer has been installed within the 70° sector [Fig. 2(b)]. This will enable (γ,e+ion) and (γ,2e+ion) studies to be undertaken, in addition to (γ,2e) experiments. The new geometrical constraints required a system to admit the gas coaxially with the photon beam. The general ''design concept,'' inspired by the conical systems of Kammerling and Schmidt,[21] and Yagishita and co-workers,[22] was that of a circular array of gas tubes of one or more layers which surround an axial photon beam. The gas tubes could be set slightly off axis so that they all effectively lie on the surface of a cone, thus creating a focus in the resulting beam. The system was designed so that the number of molecules (target number; TN) within the interaction region would be greatest at approximately 2–3 mm from the exit plane of the array. This was considered to be the best way to maintain a high pressure differential between the chamber and an UHV photon source, and minimize the detection of low energy electrons ejected from the surfaces of the gas tubes. It was decided therefore that the parameters of the array should be selected by modeling the gas flow and optimizing for these criteria. Sections II and III describe the calculations performed. Section IV details the design and construction, and Sec. V gives evidence of its initial performance.

[a]Author to whom correspondence should be addressed; electronic mail: d.p.seccombe@newcastle.ac.uk

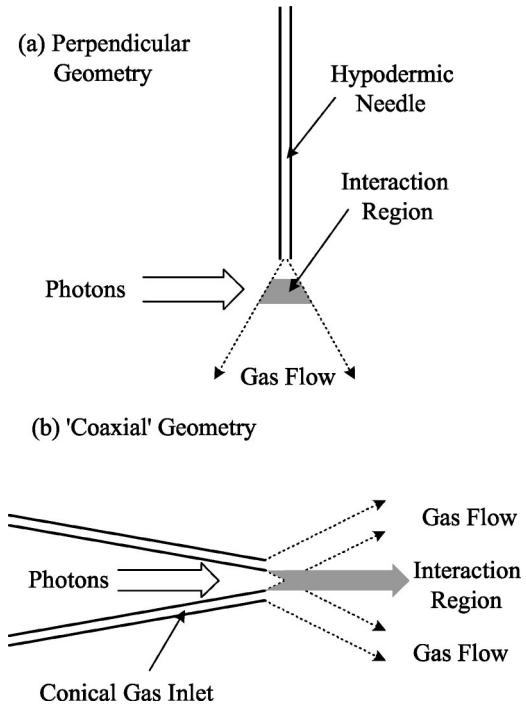

FIG. 1. Idealized shapes of gas–photon interaction regions for (a) perpendicular and (b) the ''coaxial'' geometries.

II. THEORY

A. Preliminaries

There have been many attempts both theoretically and experimentally to determine gas densities associated with an effusive source.[4–19,23–33] Our interest here lies in modeling the molecular density beyond the exit plane of the source. The approach taken is to use the theory derived by Olander and Kruger[8] for calculating gas densities arising from a single tube and to extend it to a conical array of capillaries (Secs. II B and II C). Before describing this process, however, the basic properties of the system(s) are discussed.

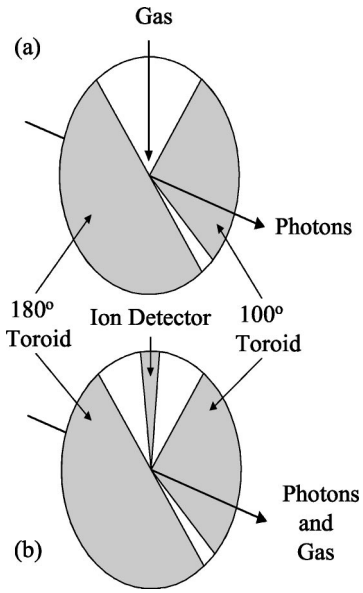

FIG. 2. Schematic depicting the angular acceptances of the analyzers: (a) The original configuration comprising the two toroidal analyzers. Gas is admitted into the chamber perpendicularly to the direction of the photon beam. (b) The new arrangement; an additional cylindrical analyzer has been added. Due to a lack of space within the detection plane, the photons and gas have to enter the system along the same path.

TABLE I. Reservoir pressure, P_1, for free molecular flow conditions for several gases with 0.25-mm-diam tubes.

Gas	Mass number	Collisional cross section, σ (nm^2)[a]	Reservoir pressure, P_1 (Torr) when $\mathrm{Kn}_d=0.3$
H_2	2	0.27	1.1
He	4	0.21	1.4
N_2	28	0.43	0.7
O_2	32	0.40	0.7
Ar	40	0.36	0.8
Cl_2	70	0.93	0.3

[a]Values taken from Ref. 34.

The extent of collimation in the gas beam is determined by the radius, α, and length, l, of the tube(s) and the pressure of gas in the entrance reservoir, P_1. The flow type is inferred from the Knudsen numbers

$$\mathrm{Kn}_d=\frac{\lambda}{2\alpha}, \quad \mathrm{Kn}_l=\frac{\lambda}{l}, \tag{1}$$

where λ is the mean free path of the molecules in the entrance reservoir. Free molecular flow (FMF), where the collisions the molecules make with the walls of the tube are much more significant than intermolecular collisions, occurs when $\mathrm{Kn}_d>0.3$.[33] Another important quantity is the tube's aspect ratio, γ, given by

$$\gamma=\frac{2\alpha}{l}=\frac{\mathrm{Kn}_l}{\mathrm{Kn}_d}. \tag{2}$$

The greatest collimation in the gas beam results when $\gamma\rightarrow 0$ and when the flow type is free molecular.

There are two restrictions placed on the gas pressure in the entrance reservoir (P_1). First, for free molecular flow conditions to hold, P_1 must be such that $\mathrm{Kn}_d>0.3$. For tubes with dimensions of 0.125 and 25 mm for α and l, respectively, and H_2 as the target molecule with a temperature of 298 K, the maximum value of P_1 for free molecular flow is $\sim$1 Torr (see Table I).[34] In practice this limit may be surpassed in an effort to increase the target number in the interaction region. A degree of collimation is surrendered when free molecular flow is compromised and ultimately at high pressures the target number may actually begin to *decrease*. Second, there is the practical limitation imposed by the pumps of the vacuum chamber. In our experiment, which has two 1000 l s^{-1} Leybold turbo-molecular pumps, the highest ambient pressure within the chamber, P_a, that can be tolerated is $\sim 1.6\times 10^{-4}$ Torr. This restriction on the value of P_a can be translated to an upper limit of P_1. Since the gas throughput, Q (Pa m^3 s^{-1}), at every point in a pumping cycle is constant in the steady-state situation, the throughput of the array (Q_{array}) equals that of the pump (Q_{pump}). The former is $L(P_1-P_2)$ and the latter is P_aS.[33,35] Therefore it follows that

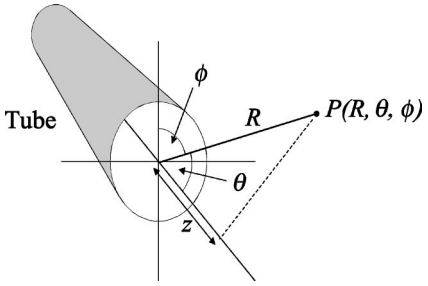

FIG. 3. The single tube scenario. $P(R,\theta,\phi)$ is a general point in space beyond the exit plane of the tube in spherical coordinates.

$$L(P_1-P_2)=P_aS, \tag{3}$$

where P_2 is the pressure of gas in the exit region of the array, S is the net pumping speed within the chamber, and L is the conductance of the array. In the free molecular flow regime, L is given by[33]

$$L=N_T\frac{2\pi\bar{c}\alpha^3}{3l}, \tag{4}$$

where $\bar{c}$ is the mean molecular speed and N_T is the number of tubes in the array. Making the (perhaps questionable) assumption that there is no significant change in the temperature of the gas during its expansion, then the flux of molecules through the exit plane of the array should equal that through the entrance plane of the turbo-molecular pumps. Consequently, P_2 can then be expressed in terms of the ambient pressure, P_a:

$$P_2=R_AP_a, \tag{5}$$

$$R_A=A_{\text{pump}}/A_{\text{array}}, \tag{6}$$

where A_{pump} is the total area of the entrance plane of the pumps and $A_{\text{array}}(=N_T\pi\alpha^2)$ is that of the exit plane of the array. Thus, P_1 can be related to P_a by

$$P_a=\frac{LP_1}{S+R_AL}. \tag{7}$$

Using $L=N_TL_1$, where L_1 is the conductance of one tube [see Eq. (4)], this equation can be rearranged in terms of P_1 to give the relationship

$$P_1=\frac{P_a}{N_T}\left[\frac{S}{L_1}+\frac{A_{\text{pump}}}{\pi\alpha^2}\right]. \tag{8}$$

Note that for a given P_a, $P_1\propto 1/N_T$ is valid for all flow regimes. The use of many tubes improves the target number, TN, for a given P_1, but Eq. (8) shows that P_1 itself depends on N_T for a constant P_a and this in turn affects the maximum TN that can be achieved. More importantly, however, is that P_1 needs to be lower than the maximum pressure for free-molecular flow for the gas beam to be well collimated.

B. The target number resulting from molecules flowing through a single tube

The angular distribution of the molecular flux ($(J\theta)$: molecules $\text{s}^{-1}\,\text{sr}^{-1}$) beyond the exit plane of the tube (Fig. 3) is given by

$$J(\theta)=v\alpha^2j(\theta), \tag{9}$$

where α is the radius of the tube, $j(\theta)$ is the distribution function, and v is the net rate at which molecules in the gas reservoir enter a unit area of the tube—given by $v=n_v\bar{c}/4$, where n_v is the number density (molecules m^{-3}) in the source reservoir. It should be noted that due to the cylindrical symmetry of the tube there is no azimuthal gas density variation. In the situation that $\tan(\theta)\geqslant\gamma$, appropriate for this study, Olander and Kruger[8] have shown that $j(\theta)$ is given by

$$j(\theta)=\xi_0\cos(\theta)\left[1+\frac{2\kappa\exp(\delta^2)}{\delta\sqrt{\pi}}\right], \tag{10}$$

where

$$\delta=\sqrt{\frac{\xi_0^2}{(\xi_1-\xi_0)\cos(\theta)2\text{Kn}_l}} \tag{11}$$

and

$$\kappa=\int_0^1\sqrt{(1-x^2)}\left(\text{erf}\left\{\delta\left[1+\frac{\gamma x}{\tan(\theta)}\left(\frac{\xi_1}{\xi_0}-1\right)\right]\right\}-\text{erf}(\delta)\right)dx. \tag{12}$$

These expressions do not make the usual assumption of zero pressure at the end of the tube and are not solely limited to the free molecular flow regime. The symbols ξ_1 and ξ_0, denote the ratio of the number densities within the entrance and exit planes of the tube, to that within the source reservoir. These quantities are related to the dimensionless impingement rates upon the walls of the tube, ς_1 and ς_0, which take the values 1 and 0.666γ in the limit $\gamma\rightarrow 0$.[36] Olander and Kruger[8] have determined the corresponding values for ξ_1 and ξ_0 to be 1.223 and 0.515γ, respectively, and it is these numbers we have used.

The gas density, ρ (molecules $\text{m}^{-3}\,\text{sr}^{-1}$), as a function of the polar coordinates defined in Fig. 3, is given by

$$\rho(R,\theta,\phi)=\frac{J(\theta)}{\bar{c}R^2}. \tag{13}$$

If the size, shape, and position of the interaction region is known, then once the gas density at all points has been determined, the number of molecules within the interaction region (target number; TN) can be calculated. In this situation the interaction region has a simple cylindrical geometry, symmetric about the C_∞ axis of the tube (provided the divergence of the radiation is insignificant). The radius of the cylinder (r_i) is equal to that of the beam of radiation and its length is denoted by l_i. The target number (TN) is given by

$$TN=2\pi\int_{Z_0}^{Z_1}\int_0^{\chi}\frac{J(\theta)z\tan(\theta)}{\bar{c}R^2}d\theta\,dz, \tag{14}$$

where

$$R=\frac{z}{\cos(\theta)}, \tag{15}$$

$$\chi=\tan^{-1}\left[\frac{r_i}{z}\right], \tag{16}$$

and

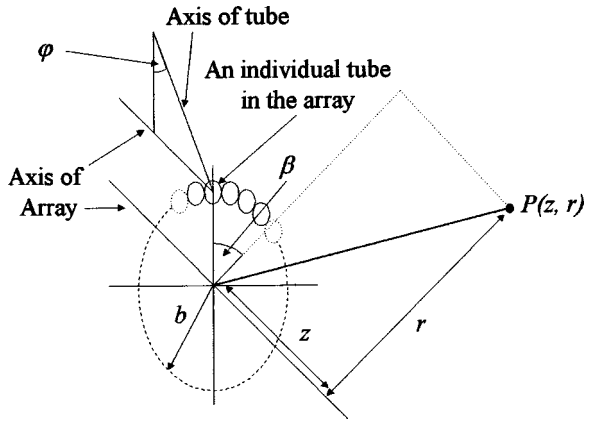

FIG. 4. A schematic showing the orientation of an array of tubes arranged with exit apertures lying in a circle and axes lying on a cone. The term φ denotes the tilt angle and β defines the angular position of a tube within the array. $P(z,r)$ is a general point in space beyond the exit plane of the array defined by a coordinate system with an origin at the center of the array.

$$Z_1 = Z_0 + l_i. \tag{17}$$

The symbol, z, represents the projection of R along the tube axis (see Fig. 3) and Z_0 is the distance on axis from the tube exit to the entrance of the interaction region.

C. Extension to several tubes arranged in a hollow conical array

Figure 4 shows the situation where several tubes are arranged in a circle of radius b, with their axes lying on the surface of a cone. The number of tubes in the array, N_T, is approximated by

$$N_T \approx \frac{\pi b}{\alpha + \Delta\alpha}, \tag{18}$$

where α ($\alpha \ll b$) is the internal radius of an individual tube and $\Delta\alpha$ is the tube wall thickness. The tilt angle, φ, lies between the axes of the individual capillaries and the plane perpendicular to the C_∞ axis of the array while β defines the angular position of an individual capillary within the array. If it is assumed that the molecular distributions from the individual tubes are independent of one another, then the total molecular density at a given point in space can be determined by adding the contributions from each individual capillary. This approach has been used successfully by Brinkmann and Trajmar[12] to determine the molecular densities from conventional multicapillary arrays. Equation (13) was derived in terms of θ and R, where these parameters define a position in space relative to an individual capillary. Here, we require a coordinate system that defines a position in space relative to the whole array, i.e., z, the distance, along the C_∞ axis of the array, from the plane of the tube axis, and r, the distance from the C_∞ axis of the array (see Fig. 4). R and θ are related to z and r by

$$R = \sqrt{r^2 + b^2 - 2rb\cos(\beta) + z^2}, \tag{19}$$

$$\theta = \cos^{-1}\left[\frac{b^2 - br\cos(\beta) + bz\tan(\varphi)}{\sqrt{b^2 + [b\tan(\varphi)]^2}R}\right]. \tag{20}$$

The gas density at a given point beyond the exit plane of the array $\rho(z,r)$, can be approximated by

$$\rho(z,r) \approx b\int_0^{2\pi} \frac{\rho_i[R(z,r,\beta),\theta(z,r,\beta)]}{2(\alpha+\Delta\alpha)}\,d\beta, \tag{21}$$

where R and θ are given by Eqs. (19) and (20) and ρ_i is the contribution to the total density from a single tube in the array. The resulting equation simplifies to

$$\rho(z,r) \approx \frac{N_T}{2\pi}\int_0^{2\pi} \rho_i[R(z,r,\beta),\theta(z,r,\beta)]\,d\beta \tag{22}$$

using Eq. (18). The number of molecules (TN) within a cylindrical interaction region, whose C_∞ axis is the same as that of the array, can be calculated using:

$$TN = 2\pi\int_{Z_0}^{Z_1}\int_0^{r_i} \rho(z,r)\,r\,dr\,dz. \tag{23}$$

It is possible to extend this theory to include two or more layers in the array. The radius of the smallest circle is now defined as b_1. The radii of the other layers b_n are given by

$$b_n = b_1 + 2(n-1)(\alpha+\Delta\alpha), \tag{24}$$

where n is the index of the layer. If it is assumed that the molecular distributions due to each layer are independent of one another, then the TN for a multilayered system is given by

$$TN = 2\pi\sum_{n=1}^{N}\int_{Z_0}^{Z_1}\int_0^{r_i} \rho(z,r,n)\,r\,dr\,dz, \tag{25}$$

where N is the number of layers in the array. Note that the problem reduces to that of a conventional multicapillary array when $b_1 = 0$ and $\varphi = 90°$.

III. CALCULATIONS

A. Single tube

Since the immediate aim of the experiment was to probe photodouble ionization of H_2 (or D_2), this molecule is used exclusively in the calculations. In order to demonstrate the advantage of using an array of tubes arranged in the manner described above, a calculation for a single tube located on axis was first performed. The dimensions of the tube were set to 0.125 and 25 mm, for the radius and length, respectively, corresponding to an aspect ratio of 0.01. This is close to the limit, $\gamma \to 0$, without the pressure difference between the entrance and exit planes being too great. The pressure in the source reservoir was set to 1 Torr since this is the highest pressure in the free molecular flow regime ($Kn_d = \sim 0.3$). In all cases a temperature of 298 K was used. The target number (TN) was calculated [using Eq. (14)] as a function of Z_0 for a 1-mm-long cylindrical interaction region (radius=1 mm) and the results are shown in Fig. 5. The figure confirms what is intuitively obvious, that TN decreases as Z_0 increases. This would create a great deal of secondary emission in the hypothetical case of genuine coaxial and photon beams.

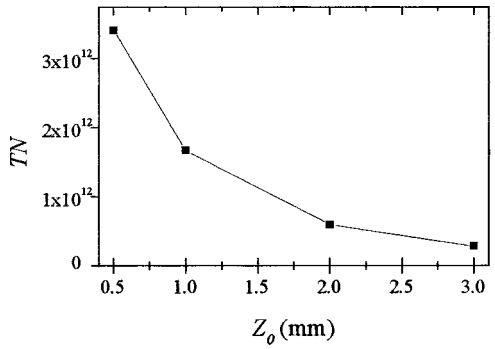

FIG. 5. The target numbers (TN) for several cylindrically shaped interaction regions (of 1 mm length and radius) located on axis at various distances (Z_0) from the exit plane of a single tube.

B. Array of tubes arranged in a conical geometry

A calculation for the situation of an array of tubes arranged in a cone was performed using Eq. (23). The dimensions of the interaction region and individual capillaries, the identity of the gas, the pressure, and temperature in the source reservoir are all identical to the single tube situation. The thickness of the tube walls ($\Delta\alpha$) was set to 0.05 mm. The target numbers for systems with $b=2$, 3, 4 mm were calculated for $\varphi=35°$–$90°$ and $Z_0=0.5$–3 mm [Figs. 6(a)–6(c)]. In all cases only one layer of tubes is considered.

From the figure it is possible to draw two conclusions. First, for a given b, as φ increases, the peak of the function shifts to a larger Z_0 and the TN in the peak decreases. A similar trend is observed as b is increased for a given φ. Second, even if both b and φ are adjusted simultaneously, it is not possible to shift the peak to a *significantly* greater Z_0 without lowering the TN. Hence the choice of Z_0 for the peak is critical. It rests on a compromise between a high TN (small Z_0) and a low risk of background counts (large Z_0). Since the latter of the two effects is difficult to quantify, our choice of 3 mm for Z_0 is based on intuition rather than calculation. We therefore required a combination of b and φ that maximizes the TN ($Z_0=3$ mm), while ensuring that the TNs ($Z_0<3$ mm) are lower than this in order to both minimize the noise and maintain the necessary pressure differential with the photon source region. It appears that $\varphi=45°$ is the best tilt angle but, from these calculations alone with only a limited set of data points, it is not possible to discern an optimum array radius (b). Thus a more comprehensive set of calculations, over a larger range of Z_0 and b, was performed for this tilt angle (Fig. 7).

It is evident that for a peak at $Z_0=3$ mm, a radius (b) of 4 mm is required. In this situation the TN is $\sim 4.5\times10^{10}$ mol. If a peak at $Z_0=2$ mm is considered satisfactory ($b=3$ mm), then a TN of greater than 5×10^{10} mol can be obtained.

C. The many-layer situation

In the many-layer case, the effect of the ambient pressure should also be considered. While increasing N_T increases the target number for a given P_1, it also increases P_a. The consequence of this is to reduce the maximum practical value of P_1. In Sec. II A it was shown that P_1 is inversely proportional to N_T [Eq. (8)]. Hence, when considering a large N_T, which is likely to arise when many layers are considered, it is more appropriate to use the ratio TN/N_T rather than TN alone. Calculations were performed for 1–9 layers ($\varphi=45°$) with $\Delta\alpha$ at the more realistic value of 0.125 mm and the radius of the interaction region set to 0.5 mm; otherwise the parameters were as above. Four conditions were considered, the results for which are shown in Fig. 8.

If a large TN at $Z_0=2$ mm, rather than the more desirable $Z_0=3$ mm, is considered satisfactory, then a two-layer

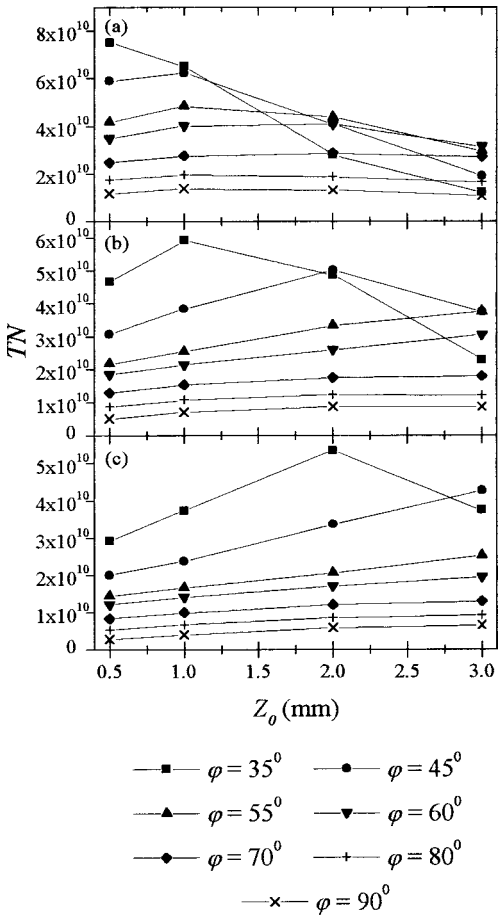

FIG. 6. The target numbers (TN) for several cylindrically shaped interaction regions (of 1 mm length and radius) located on axis at various distances (Z_0) from the exit plane of several single-layered conical arrays: (a) $b=2$ mm $\varphi=35°$–$90°$ (b) $b=3$ mm $\varphi=35°$–$90°$ (c) $b=4$ mm $\varphi=35°$–$90°$.

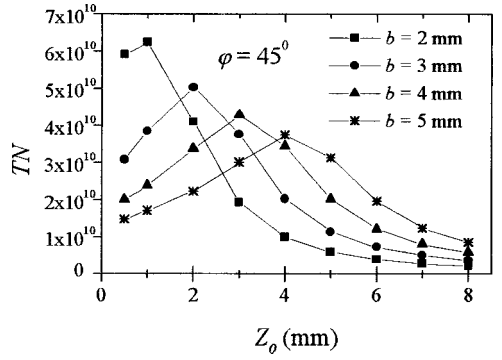

FIG. 7. The target numbers (TN) of single-layered conical arrays as a function of (Z_0), as in Fig. 6, but with $\varphi=45°$.

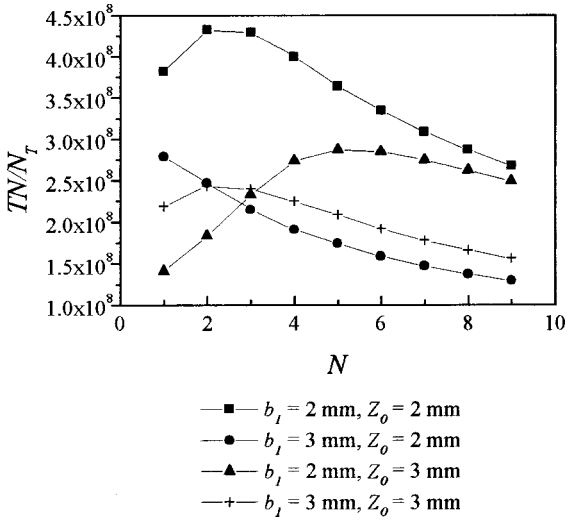

FIG. 8. The TN/N_T ratios for several cylindrically shaped interaction regions (of 1 mm length and 0.5 mm radius) located on axis at various distances (Z_0) from the exit plane of several multilayered conical arrays.

system with a minimum radius of 2 mm appears to be best. This conclusion, however, is drawn without considering the characteristic of the flow. In this analysis a two-layer system ($b_1=2$ mm) has 50 capillaries while a three-layer system has 75, a significant increase considering there is only a marginal difference in TN/N_T between the two. Hence the three-layer system is preferred since the increased number of capillaries ensures that there is a larger range for free molecular flow and, consequently, the device construction is based on this design.

IV. DESIGN AND CONSTRUCTION

A frontal view of the three-layered gas injection system is shown in Fig. 9. It was constructed from aluminum, chosen because of its relative ease of machining and nonmagnetic properties. In total, 90 grooves ($2\alpha=0.25$ mm) were cut into three conical surfaces. The open edge of each groove was then sealed by the inside surface of the adjacent cone allowing each groove to behave as an independent capillary. A solid conical lid is provided for the outermost layer of grooves. It should be noted that the grooves have a square-shaped cross section, whereas the theoretical analysis was performed using cylindrical tubes. For free molecular flow (FMF), where collisions with the tube walls dominate over intermolecular collisions, this change in tube geometry is not particularly significant as the tube's wall area-to-volume ratio is the same for both cross sections. However, the symmetry in the angular distributions about the tube axis decreases when the cross section changes from a circle to a square. This effect will perturb the predicted density distributions and needs to be borne in mind when making quantitative comparisons between performance and theory.

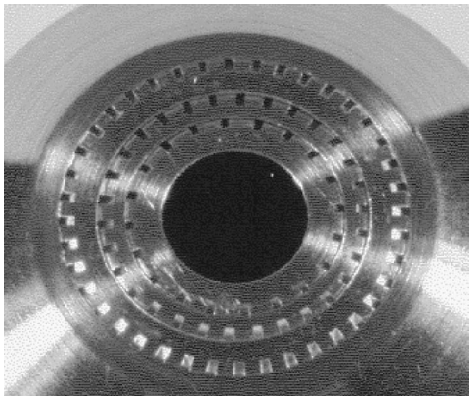

FIG. 9. A photograph of the front of the recently constructed three-layered effusive source. The 90 grooves each have a width of 0.25 mm and the central hole for photons has a 4 mm diameter.

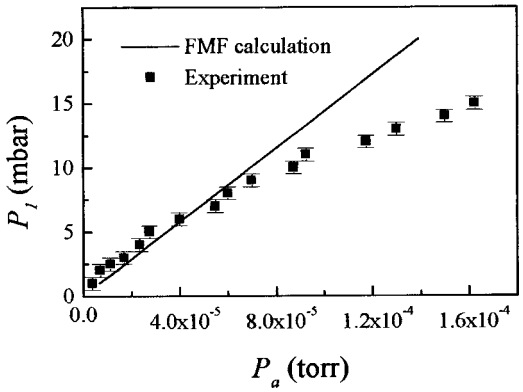

FIG. 10. The relationship between the pressure in the source reservoir (P_1) and the ambient pressure within the chamber (P_a) for D_2 ($M=4$, $\sigma=0.27$ nm^2) (see Ref. 34). The line was produced using Eq. (7) with a free molecular flow conductance and the squares represent experimental measurements.

The photon beam enters the vacuum chamber through the 4-mm-diam orifice in the center of the device. The tilt angles, φ, employed were 55°, 45° and 35°, for layers 1–3, respectively. Since each groove must be ~25 mm long, due to the limited radial space available, the grooves adopt a $\varphi=90°$ orientation ~4 mm from the tube exit. The ''bend'' in the tube will obviously alter the flow characteristics and may reduce the degree of collimation, effectively slightly increasing the aspect ratio. Even so, initial tests of the device (Sec. V) show that γ remains sufficiently close to zero for the model to hold.

The entrance reservoir consists of a simple two stage mixing section to provide isotropy in the gas flow. Gas, from a high precision needle valve, enters the system through Teflon tubing. The device is mounted on a linear drive so that the exit plane of the array can be varied in laboratory space. For the preliminary experiments the position was set 2.5 mm away from the center of the mechanical field of view of the analyzers.

V. DISCUSSION

A. The relationship between P_1 and P_a

Using D_2 as the target gas, P_1 was measured for several values of P_a to test the range of validity of FMF. P_a was measured with an ion gauge (Vacuum Generators: VIG 8) and P_1 with a barometrically compensated mechanical gauge (Edwards: CG3). The results can be compared with those obtained using Eq. (7), L and S being set to 1.856×10^{-5} and 2.0 $m^3 s^{-1}$, respectively, and R_A to 3.395×10^4 (Fig. 10).

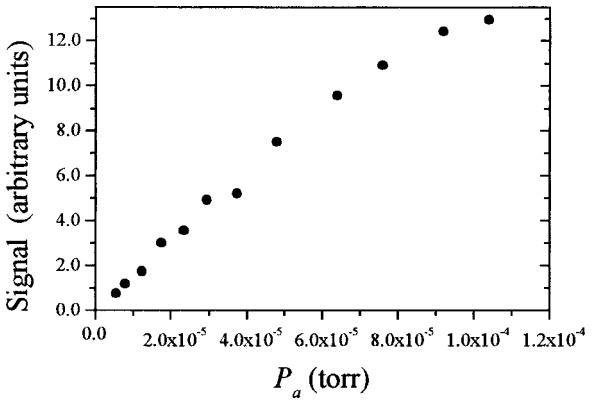

FIG. 11. A plot of the photoionization signal arising from the $h\nu(54.5\,\mathrm{eV})+\mathrm{He}(2s^2)\rightarrow\mathrm{He}^+(2s^1)+\mathrm{e}^-(30\,\mathrm{eV})$ transition as a function of the ambient pressure within the chamber (P_a). The 30 eV electrons were detected by the cylindrical analyzer shown in Fig. 2(b).

Inspection of the graph reveals that the FMF model holds below $P_1\sim 7$ mbar ($\mathrm{Kn}_d>0.062$). The slight displacement between theory and experiment is probably due to uncertainty in the actual values of P_a, R_A, and S. Above $P_1\sim 7$ mbar, the relationship between P_1 and P_a departs from linearity indicating the onset of pressure dependence in the array conductance (L). The direction of curvature indicates that L increases with P_1, which is consistent with Poiseuille flow behavior at low Knudsen numbers.[33] At the maximum practical ambient pressure, 1.6×10^{-4} Torr, the FMF regime is significantly exceeded and should result in a loss of gas beam collimation. This is confirmed in Fig. 11, which reveals saturation in the photoelectron count rate at high pressure.

B. Focusing properties

The focusing properties of the gas jet were tested by measuring the electron yield, arising from the single photoionization of helium, as a function of position within the chamber. Photons ($h\nu=54.5\,\mathrm{eV}$) were supplied by a synchrotron and 30 eV electrons produced by the $\mathrm{He}(2s^2)\rightarrow\mathrm{He}^+(2s^1)$ transition were detected using the cylindrical analyzer [Fig. 2(b)]. The sampled region of space was varied within the horizontal plane by changing the voltages of two mutually orthogonal deflectors ($D1$ and $D2$) at the entrance to the energy-dispersive analyzer. Each deflector is situated 45° from the photon beam axis and acts so that decreasing the voltage on $D2$ while increasing that on $D1$ moves the analyzer's viewpoint away from the surface of the gas inlet (see Fig. 12). It was not possible to map the voltages (V), or voltage differences (ΔV) onto an absolute position scale due to the complexity of the electron optics. A three-dimensional spectrum of signal versus $D1$ and $D2$ is shown in Fig. 12 and clearly displays the focus of the gas beam. It also shows that the focus position is at some distance away from the surface of the gas inlet system; if this were not so the signal would not go through a maximum on the photon beam axis. Thus we can be assured that the problems associated with surface emission are minimized. The apparent defects in the image could arise from three factors; (a) small electric fields penetrating the interaction region, (b) insufficient mixing in the gas injection system, or (c) aberrations of the photon beam. It is also quite possible that intermolecular collisions should not be ignored within the focal region as these could perturb the gas flow beyond that point.

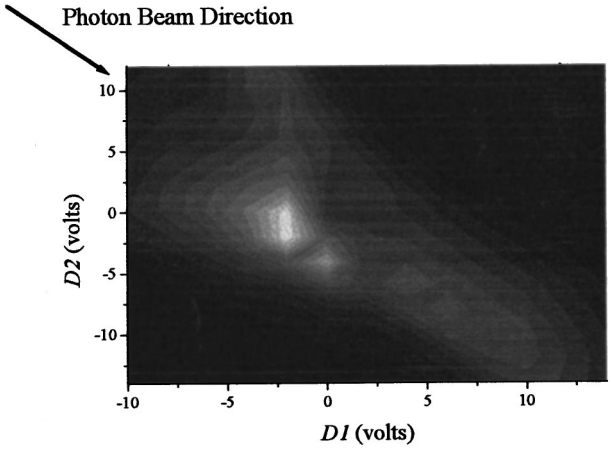

FIG. 12. A contour plot of the photoionization signal arising from the $\mathrm{He}(2s^2)\rightarrow\mathrm{He}^+(2s^1)$ transition as a function of deflector voltages ($D1$ and $D2$). The ambient pressure within the chamber was 4×10^{-5} Torr.

C. Initial result

As mentioned in Sec. I, this work was motivated by the desire to investigate electron-ion/electron correlation effects resulting from photodouble ionization (PDI) of H_2. In these initial experiments—where D_2 was used for logistical reasons—photons ($h\nu=76.1\,\mathrm{eV}$) from the SU6 undulator beamline (SuperACO, France) were used to doubly ionize the molecules. Since the D_2 PDI threshold is 51.1 eV, the excess energy shared between the two electrons is 25 eV. Immediately following double ionization, the two D^+ ions recoil rapidly in the ''Coulomb explosion'' and the kinetic energy released during this process is ~18.8 eV. Since this dissociation is so fast, the angle resolved detection of a D^+ fragment in coincidence with one or two of the electrons enables studies of ''fixed-in-space'' molecules. Coincidence

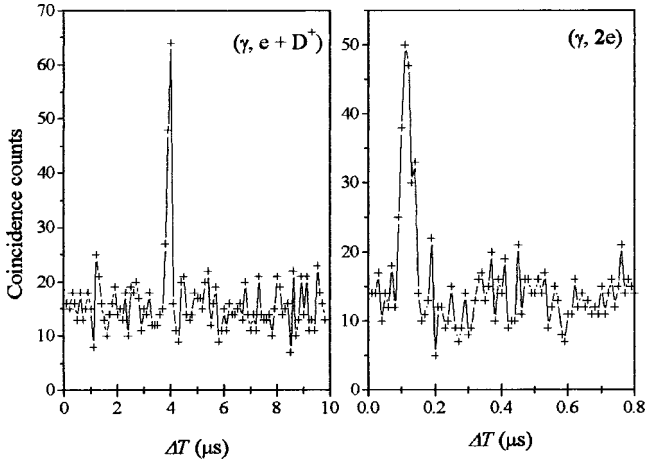

FIG. 13. Time correlation spectra for $D_2(h\nu=76.1\,\mathrm{eV})$ showing the ''true'' coincidence peak on a uniform random background for coincidences between (a) 20 eV electrons from the large toroidal and 9 eV D^+ ions from the cylindrical analyzer, and (b) 20 and 5 eV electrons detected by the two toroidal analyzers. Typical count rates were ~20 true events per hour.

measurements of the PDI of D_2 were taken using the spectrometer described in Sec. I with the arrangement of the three analyzers as shown in Fig. 2(b). The two toroidal analyzers were tuned to detect electrons while the cylindrical analyzer was tuned for ~9 eV ions. The energies of the detected electrons were 5 and 20 eV for the small and large toroids, respectively. Coincidence spectra of these initial ion-electron $(\gamma, D^+ + e^-)$ and electron–electron $(\gamma, 2e^-)$ measurements, recorded in parallel, are shown in Fig. 13. The $(\gamma, 2e)$ angular distribution measurements are reported elsewhere.[37]

ACKNOWLEDGMENTS

This work was done with financial assistance from EPSRC and the initial experiments were performed at LURE with further support from the EU Large Scale Facilities Program. The authors would like to thank Alan Bott, Andrew Kerr, and John Corner for their skill and ingenuity in the mechanical design and construction of the gas source. The authors acknowledge the invaluable insight obtained from an earlier version of the system designed by Jim Wightman and Slobodan Cvejanović. Finally, the authors would like to thank Volker Schmidt, Alain Huetz, and Akira Yagishita for stimulating discussions and advice.

[1] J. P. Gordon, H. Zeiger, and C. H. Townes, Phys. Rev. **99**, 1264 (1955).
[2] J. G. King and Z. R. Zacharias, Adv. Electron. Electron Phys. **6**, 1 (1956).
[3] J. C. Helmer, F. B. Jacobs, and P. A. Sturrock, J. Appl. Phys. **31**, 458 (1960).
[4] J. A. Giordmaine and T. C. Wang, J. Appl. Phys. **31**, 463 (1960).
[5] G. R. Hanes, J. Appl. Phys. **31**, 2171 (1960).
[6] R. H. Jones, D. R. Olander, and V. R. Kruger, J. Appl. Phys. **40**, 4641 (1969).
[7] D. R. Olander, J. Appl. Phys. **40**, 4650 (1969).
[8] D. R. Olander and V. Kruger, J. Appl. Phys. **41**, 2769 (1970).
[9] C. B. Lucas, Vacuum **23**, 395 (1973).
[10] H. C. W. Beijerinck and N. F. Verster, J. Appl. Phys. **46**, 2083 (1975).
[11] S. K. Srivastava, A. Chutjian, and S. Trajmar, J. Chem. Phys. **63**, 2659 (1975).
[12] R. T. Brinkmann and S. Trajmar, J. Phys. E **14**, 245 (1981).
[13] H. P. Steinrück and K. D. Rendulic, Vacuum **36**, 213 (1986).
[14] A. M. Glines, R. N. Carter, and A. B. Anton, Rev. Sci. Instrum. **63**, 1826 (1992).
[15] S. J. Buckmann, R. J. Gulley, M. Moghbelalhossein, and S. J. Bennet, Meas. Sci. Technol. **4**, 1143 (1993).
[16] B. Bapat and E. Krishnakumar, Z. Phys. D: At., Mol. Clusters **31**, 1 (1994).
[17] D. E. Kuhl and R. G. Tobin, Rev. Sci. Instrum. **66**, 3016 (1995).
[18] Y. Ma, B. Y. H. Liu, H. S. Lee, K. Mauersberger, and J. Morton, J. Vac. Sci. Technol. A **14**, 2414 (1996).
[19] J. M. Guevremont, S. Sheldon, and F. Zaera, Rev. Sci. Instrum. **71**, 3869 (2000).
[20] T. J. Reddish, G. Richmond, G. W. Bagley, J. P. Wightman, and S. Cvejanović, Rev. Sci. Instrum. **68**, 2685 (1997).
[21] B. Kammerling and V. Schmidt, J. Phys. B **26**, 1141 (1993).
[22] A. Yagishita (private communication).
[23] P. Clausing, Z. Phys. **66**, 471 (1930).
[24] P. Zugenmaier, Z. Angew. Phys. **20**, 184 (1965).
[25] L. M. Lund and A. S. Berman, J. Appl. Phys. **37**, 2489 (1966).
[26] L. M. Lund and A. S. Berman, J. Appl. Phys. **37**, 2496 (1966).
[27] G. C. Angel and R. A. Giles, J. Phys. B **5**, 80 (1972).
[28] C. M. Davies and C. B. Lucas, J. Phys. D **16**, 1 (1983).
[29] W. Steckelmacher and K. F. Man, Rev. Sci. Instrum. **56**, 58 (1985).
[30] S. Adamson and J. F. Mcgilp, Vacuum **36**, 227 (1986).
[31] S. Adamson, C. O'Carroll, and J. F. Mcgilp, Vacuum **38**, 463 (1988).
[32] D. M. Murphy, J. Vac. Sci. Technol. A **7**, 3075 (1989).
[33] V. Schmidt, *Electron Spectrometry of Atoms using Synchrotron Radiation*, *Cambridge Monographs on Atomic, Molecular and Chemical Physics* (Cambridge University Press, Cambridge, 1997), Vol. 6.
[34] *Tables of Physical and Chemical Constants*, edited by G. W. C. Kaye and T. H. Laby (Longman, London, 1973).
[35] K. Diels and R. Jaeckel, *Leybold Vacuum Handbook* (Pergamon, New York, 1966).
[36] P. Clausing, Ann. Phys. (Paris) **12**, 961 (1932).
[37] S. A. Collins, A. Huetz, T. J. Reddish, D. P. Seccombe, and K. Soejima, Phys. Rev. Lett. (submitted).